Engineering 6 (2020) 637–643

Contents lists available at ScienceDirect

Engineering

journal homepage: www.elsevier.com/locate/eng

Research
Materials Genome Engineering—Article

Combinatorial Synthesis and High-Throughput Characterization of Microstructure and Phase Transformation in Ni–Ti–Cu–V Quaternary Thin-Film Library

Naila M. Al Hasan [a], Huilong Hou [a], Suchismita Sarkar [b], Sigurd Thienhaus [c], Apurva Mehta [b], Alfred Ludwig [c], Ichiro Takeuchi [a,*]

[a] Department of Materials Science and Engineering, University of Maryland, College Park, MD 20742, USA
[b] Stanford Synchrotron Radiation Lightsource, SLAC National Accelerator Laboratory, Menlo Park, CA 94025, USA
[c] Werkstoffe der Mikrotechnik, Ruhr-Universität Bochum, Bochum 44801, Germany

ARTICLE INFO

Article history:
Received 3 June 2019
Revised 10 October 2019
Accepted 24 December 2019
Available online 16 May 2020

Keywords:
Ni–Ti–Cu–V alloys
Combinatorial materials science
Quaternary alloys
Shape memory alloys
Thin-film library
Elastocaloric cooling
Thermoelastic cooling
Phase transformation
High-throughput characterization
Property mapping
Machine learning

ABSTRACT

Ni–Ti–based shape memory alloys (SMAs) have found widespread use in the last 70 years, but improving their functional stability remains a key quest for more robust and advanced applications. Named for their ability to retain their processed shape as a result of a reversible martensitic transformation, SMAs are highly sensitive to compositional variations. Alloying with ternary and quaternary elements to fine-tune the lattice parameters and the thermal hysteresis of an SMA, therefore, becomes a challenge in materials exploration. Combinatorial materials science allows streamlining of the synthesis process and data management from multiple characterization techniques. In this study, a composition spread of Ni–Ti–Cu–V thin-film library was synthesized by magnetron co-sputtering on a thermally oxidized Si wafer. Composition-dependent phase transformation temperature and microstructure were investigated and determined using high-throughput wavelength dispersive spectroscopy, synchrotron X-ray diffraction, and temperature-dependent resistance measurements. Of the 177 compositions in the materials library, 32 were observed to have shape memory effect, of which five had zero or near-zero thermal hysteresis. These compositions provide flexibility in the operating temperature regimes that they can be used in. A phase map for the quaternary system and correlations of functional properties are discussed with respect to the local microstructure and composition of the thin-film library.

1. Introduction

Shape memory alloys (SMAs) of nickel-titanium (Ni-Ti) are functional materials with thermal (one-way effect, 1-WE) and mechanical (pseudoelasticity, PE) "memory" [1]. This property, also known as the shape memory effect (SME), is a result of a first-order, diffusionless, and reversible phase transformation between austenite and martensite structures. When cooling from high temperature, phase transformation from austenite to martensite is characterized by the martensite start (M_s) and finish (M_f) temperatures. Similarly, the reverse process is characterized by the austenite start (A_s) and finish (A_f) temperatures. A thermal hysteresis ΔT occurs when there is a difference in the temperature at which 50% of the material is transformed into martensite upon cooling and 50% into austenite upon heating, so that $\Delta T = A_f - M_s$ [2]. Transformation temperatures (A_f) range between 0 and 100 °C for commercial NiTi alloys with a hysteresis width of 25 to 40 °C [3]. Austenitic and martensitic NiTi structures have cubic B2 and monoclinic B19' crystal lattices, respectively [1,4,5]. In addition, intermediate structures such as rhombohedral or trigonal R-phase and B19 facilitate geometric compatibility during transformation. Phases and crystal lattices present in the Ni–Ti system are extensively studied, but undesirable functional and structural properties including the strong dependence of transformation temperatures on composition and, hence, tight control of synthesis parameters present a significant challenge in their adoption into new technology [6–10]. Nonetheless, Ni–Ti SMAs enjoy widespread applications ranging from actuators, stents, orthodontics, and sensors to eco-friendly refrigeration and even fashion [11–17].

* Corresponding author.
E-mail address: takeuchi@umd.edu (I. Takeuchi).

https://doi.org/10.1016/j.eng.2020.05.003

The transformation temperature regime is a critical parameter in determining the application of SMAs along with their functional fatigue. The addition of ternary and quaternary alloying elements enables the modification and fine-tuning of the material transformation temperature for specific applications [4,9,18]. Combinatorial materials science merges the synthesis of thin films with high-throughput characterization, which allows access to many compounds covering a substantial compositional space with different stoichiometries under identical conditions. Hence, it enables the rapid discovery and development of new materials with targeted properties [19].

In this study, we report on a systematic workflow for the rapid determination of composition–structure–property relationships using combinatorial synthesis and high-throughput experimentation. We report on new Ni–Ti–Cu–V quaternary thin-film compositions having near-zero thermal hysteresis, as determined by high-throughput resistance measurements. Compositional and structural characterization was carried out with wavelength dispersive spectroscopy and high-throughput synchrotron X-ray diffraction (HiTp-XRD). A composition-phase map for the quaternary alloy was developed through automated data analysis employing hierarchical clustering techniques. This work validates theoretical predictions and builds on experimental efforts in developing new SMAs [20,21].

2. Experimental approach

Experiments were carried out with the long flat edge of the wafer positioned at the bottom so that the first set of five sample pads, labeled 1–5 from left to right, were parallel to the edge. This eased and streamlined data management.

2.1. Thin-film synthesis with magnetic sputtering

A quaternary thin-film composition spread for Ni–Ti–Cu–V between 150 and 250 nm thick was deposited on a 3 in (76.2 mm) thermally oxidized (2 μm SiO_2) silicon (Si) wafer (thickness 400 μm, IWS; International Wafer Service, Inc., USA), in an ultrahigh-vacuum (5×10^{-7} torr, 1 torr = 133.32237 Pa), magnetron sputtering system at room temperature. High-purity (99.98%) elemental targets with a diameter of 1.5 in (38.1 mm) were sputtered using DC (direct current from Seren IPS Inc., USA) and RF (radio frequency from Advanced Energy Industries, Inc., USA) power sources with an ultrahigh purity argon (Ar) (99.9997%; Airgas, USA) pressure of 5×10^{-3} torr. Each wafer was covered with a patterned Si mask to delineate 177 individual compositions evenly across the wafer at a Δx, Δy of 4.5 mm. The substrate was water cooled to avoid crystallization during sputter deposition and to maintain low temperatures. The resulting film was annealed in a vacuum at 500 °C for 1 h following the process reported in the literature [21]. Deposition rates were determined for each element used in this work under a given power source for a preset time and are listed in Table S1 of the Supplementary data. Thickness was measured using atomic force microscopy (AFM). Based on the calibrated deposition rates and the density of each element, the required power ratio to achieve a desired composition was determined and is listed in Table S2 of the Supplementary data. The total time for the synthesis and annealing of a thin-film library is 2 h before it is ready for characterization.

2.2. Chemical composition determination

Composition variation in the thin-film library was determined using wavelength dispersive X-ray (WDX) analysis in an electron probe microanalyzer (EPMA) JXA 8900R Microprobe (Microprobe, USA), with an acceleration voltage of 15 kV. Standardization of references was carried out with pure metal references and compositions were determined to be within an experimental error of < 0.3 at%.

2.3. Crystal structure analysis

Structural information was obtained at room temperature by collecting two-dimensional (2D) X-ray diffraction (XRD) patterns on the combinatorial library at beamline 1–5 at the Stanford Synchrotron Radiation Lightsource (SSRL). The experiment was performed with 14.99 keV energy collimated to approximately 0.3 mm × 0.3 mm beam size and a wavelength of 0.82657 Å (8.2657×10^{-9} m). MarCCD detector (Rayonix, L.L.C., USA) was used to collect the data at an exposure rate of 30 s. To minimize the influence of diffraction from the silicon substrate, the library was scanned with a small grazing incidence angle of 1°–2°. The grazing incidence geometry resulted in an approximate 3 mm probe footprint on the library. An automated algorithm was used to measure the entire library with a step size of 4.5 mm.

For data analysis, the geometric parameters of the 2D detector, such as the direct beam position, tilting, rotation, and sample-to-detector distance, were extracted from a measuring-standard LaB_6 powder pattern. These parameters were used to transform the initial raw images that were acquired as a function of Q and χ in the diffraction coordinate into one-dimensional (1D) diffraction patterns by integrating and normalizing over the χ angle. The Bragg angle (2θ) is related to the scattering vector (Q) by the relationship $Q = 4\times\pi\times\sin(\theta)/\lambda$, with wavelength ($\lambda$) helping to generate a more traditional 1D spectrum (intensity vs 2θ).

2.4. Characterization of transformation temperature

Film resistance as a function of temperature, $R(T)$, was measured to determine the transformation temperature, as crystal structure changes correspond with measurable electrical and magnetic changes. Resistance was measured using a four-point probe method described by Van der Pauw in a custom-built high-throughput test stand with an automated platform of five sets of four-point probes [22,23]. The spacing between the probe tips was 500 μm and the test stand was enclosed in a box purged with nitrogen (N_2) gas. Measurements were performed between −40 and 120 °C with a heating/cooling rate of 5 °C·min^{-1} and 50 mA source current.

2.5. Cluster analysis of high-throughput data

An unsupervised machine learning algorithm was used as an exploratory data analysis tool as well as a phase mapping tool. Hierarchical cluster analysis was performed using the Pearson correlation coefficient model with criteria for similarity and dissimilarity between input data, such that data grouped into a cluster shared similar characteristics in comparison with data in other clusters [24]. For two spectra x and y having the means $\bar{x}$ and $\bar{y}$ the Pearson correlation coefficient (PCC) clustering model is defined as [25]

$$C_{xy} = \frac{\sum_{i=1}^{n}(x_i - \bar{x})(y_i - \bar{y})}{[\sum_{i=1}^{n}(x_i - \bar{x})^2 \sum_{i=1}^{n}(y_i - \bar{y})^2]^{\frac{1}{2}}}$$

It was applied to the diffraction patterns using CombiView (Anritsu, Japan), which is a MATLAB-supported data visualization platform developed by the Takeuchi group.

3. Results and discussions

In this work, we investigated the influence of composition on the structure and transformation property of quaternary

$[Ni_{36}–Ti_{52}–Cu_{12}]_{(100-x)}V_x$ alloys in thin-film form. High-throughput characterization of the composition and crystal structure was performed using wavelength dispersive spectroscopy and synchrotron X-ray diffraction, respectively. Transformation behavior was characterized using resistance measurements as a function of temperature. Machine learning using a MATLAB-based visualization platform CombiView developed in-house was used to sort compositions by diffraction patterns, and therefore structures, into clusters in order to rapidly identify constituent phases and determine phase boundaries.

3.1. Chemical composition

Automated WDS measurements were carried out on all 177 samples in the materials library. Fig. 1 shows the composition variation across the wafer, with atomic percent ranges for the four elements as follows: Ni from 21.3 at% to 58.3 at%; Ti from 23.3 at% to 57.5 at%; copper (Cu) from 12.9 at% to 24.9 at%; and vanadium (V) from 2.9 at% to 6.2 at%. The targeted composition $Ti_{41.8}Ni_{37.5}Cu_{16.0}V_{4.6}$ was obtained in the center. Distribution of the elements corresponds with the elemental target gun positions inside the sputtering chamber.

3.2. Transformation temperature determination from temperature-dependent resistance measurements

The property of interest for this library was SME determined from phase transformation curves. These were obtained by carrying out temperature-dependent resistance measurements. Phase transformation temperatures of austenitic finish (A_f), and martensitic start (M_s) were determined using the tangent method [21]. Phase transformation activity for each composition as a function of wafer position in the thin-film library is shown in Fig. 2(a). Regions of transformation indicated by curves shaped as variations of "U" and "2" were observed to be limited to the right side of the wafer. The left-half portion can be divided into two main regions: The first region encompassed many compositions in the center of the wafer with non-transforming, linear behavior; the second region was limited to compositions in the far left showing non-transforming and nonlinear behavior without clear curves. Positions and compositions clustered by SME activity are shown in Figs. 2(b) and (c), respectively, where there are reversible phase transformations with nonlinear $R(T)$ curves (yellow, teal, pink), non-transforming regions with linear curves in blue, and nonlinear curves in green and red. Phase transformation parameters of

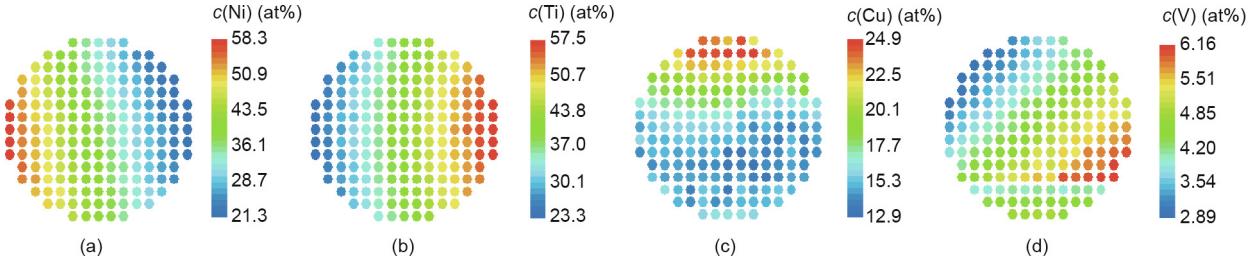

Fig. 1. Elemental distribution of (a) Ni, (b) Ti, (c) Cu, and (d) V on a 3 in Si wafer. The color scale for each element indicates composition in atomic percent from high to low indicated by the progression from red to blue. The wafer was oriented with the long flat edge at the bottom.

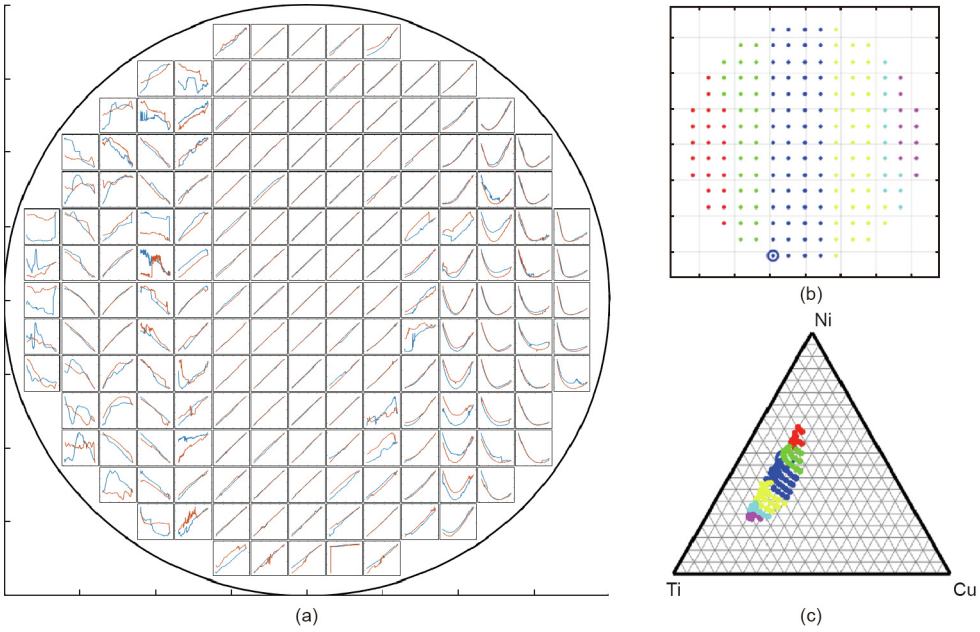

Fig. 2. (a) Temperature-dependent resistance $R(T)$ curves for $[Ni_{36}–Ti_{52}–Cu_{12}]_{(100-x)}V_x$ showing regions of transformation. Reversible transformation is observed on the right portion of the wafer as indicated by broad "U"- and "2"-shaped curves. Heating and cooling curves are indicated by red and blue colors, respectively. (b) Grouping by SME activity of wafer positions and (c) compositions projected on a ternary Cu–Ni–Ti plot, where V is between 2.9 at% and 6.2 at%.

thermal hysteresis ($\Delta T = A_f - M_s$), austenitic finish (A_f), and martensitic start (M_s) temperatures are shown in Fig. 3. All compositions with phase transformation behavior are listed in Table 1. SME was observed in 32 compositions, with five compositions having zero or near-zero thermal hysteresis and one composition having a maximum ΔT of 17.2 °C. The elemental range for compositions having SME was observed as follows: c(Ti) = 49.4 at% to 57.5 at%; c(Ni) = 21.3 at% to 30.9 at%; c(Cu) = 13.8 at% to 21.6 at%; and c(V) = 4.1 at% to 6.2 at%. The boundaries of the temperature regime where transformations to austenite occurred were observed to be centered around 13 °C to 29 °C while the martensitic start temperature was slightly reduced between 10 °C and 20 °C. Thermal hysteresis of ≤ 4 °C was observed in 19 compositions.

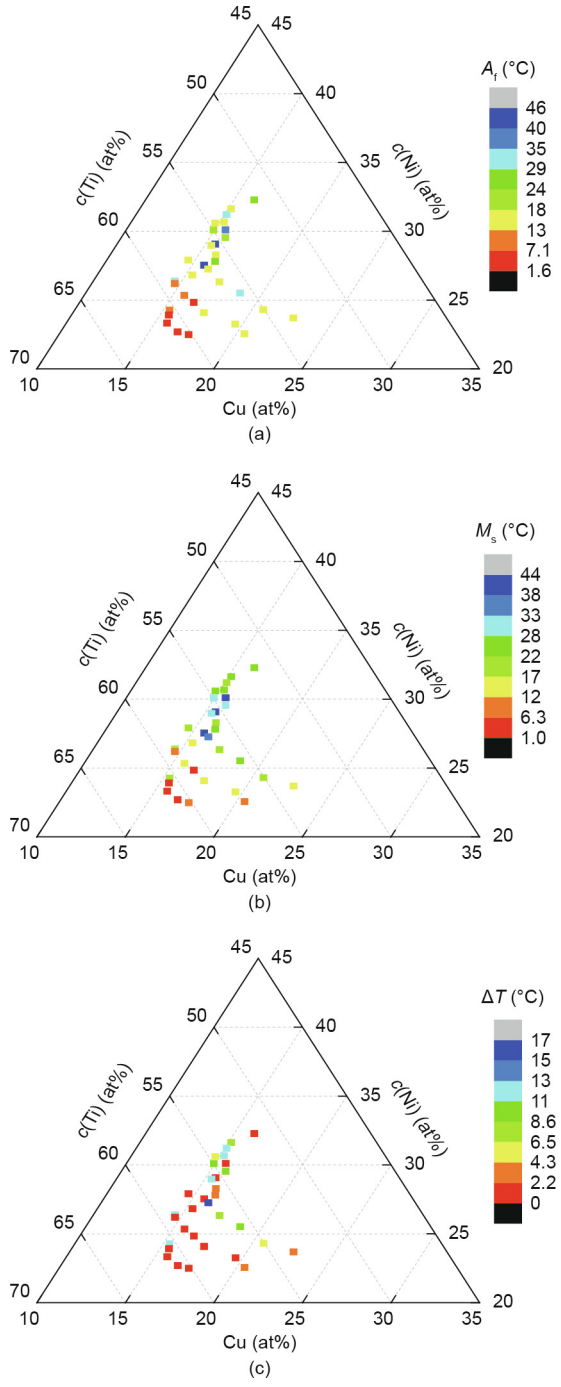

Fig. 3. Ni–Ti–Cu–V compositions having SME projected onto Cu–Ni–Ti ternary plots with the atomic concentration of V held constant between 2.9 at% and 6.2 at%. Phase transformation parameters of (a) austenitic finish (A_f) temperature, (b) martensitic start (M_s) temperature, and (c) thermal hysteresis $\Delta T = A_f - M_s$. Color scale bars from blue to red indicate high to low temperatures.

3.3. Crystal structure and phase identification

The data visualization platform CombiView allows the linking of the sample position on the wafer with its corresponding composition and diffraction pattern. The structural phase diagram was determined through a hierarchical cluster analysis of the diffraction patterns, as shown in Fig. 4. A Pearson correlation coefficient cluster analysis resulted in six clusters for the Ni–Ti–Cu–V materials library. Table 2 lists the crystal structure and space group of the phases found in the library. For non-transforming compositions, both linear and nonlinear $R(T)$ curves were observed, which were attributed to double-phase and low-symmetry crystal structures. The default structure type is a cubic phase, unless specified otherwise under prototype.

3.4. Assessment of the thin-film phase diagram

Results for the transformation properties and phases identified in the present study are listed in Table 1 and Table 2, respectively. Martensitic phase transformation determined from resistance measurement shows that the shape memory effect is limited to the Ti-rich region. SME variation changes with Ni and V content such that SME is observed to be between 21.3 at% and 33.4 at% Ni and between 4.0 at% and 6.2 at% V, respectively. This is in agreement with values reported in bulk by Frenzel et al. [9] and Schmidt et al. [26].

Clustering diffraction patterns using the Pearson correlation coefficient model match the grouping of compositions based on the shape memory behavior. Cubic NiTi with a mixture of cubic

Table 1
Thermal hysteresis, austenitic finish, and martensitic start temperatures for quaternary-Ni-Ti-Cu-V SMAs by ascending Ti content.

c(Ti) (at%)	c(Ni) (at%)	c(Cu) (at%)	c(V) (at%)	A_f (°C)	M_s (°C)	ΔT (°C)
49.4	30.9	15.5	4.2	25.0	24.0	1.0
50.0	29.7	14.3	6.0	22.8	16.0	6.8
50.6	29.4	14.2	5.8	30.0	17.5	12.5
51.0	28.9	14.4	5.7	26.5	15.2	11.3
51.2	22.6	21.6	4.5	14.4	12.0	2.4
51.7	28.9	14.0	5.4	24.0	18.0	6.0
51.7	28.0	15.1	5.2	30.7	20.4	10.3
52.0	27.3	14.6	6.2	45.6	43.5	2.1
52.0	28.5	14.1	5.4	30.6	21.7	8.9
52.1	28.9	15.0	4.1	40.0	38.0	2.0
52.4	23.1	19.7	4.8	21.2	15.2	6.0
52.5	27.3	14.5	5.7	28.8	16.4	12.4
52.5	26.7	15.1	5.8	18.0	14.0	4.0
52.9	26.3	15.3	5.5	26.8	24.0	2.8
53.0	24.2	17.8	5.0	34.4	24.8	9.6
53.3	25.8	14.7	6.1	42.9	41.9	1.0
53.6	25.0	16.3	5.1	21.2	14.4	6.8
53.7	25.8	15.2	5.3	35.2	18.0	17.2
54.2	21.5	19.5	4.9	13.6	10.0	3.6
54.2	22.1	18.6	5.1	14.8	14.0	0.8
54.3	25.2	14.4	6.1	16.0	16.0	0
54.3	26.4	13.8	5.5	19.6	17.6	2.0
55.5	22.8	16.5	5.2	13.2	12.8	0.4
55.5	24.8	13.8	5.9	29.5	17.2	12.3
55.5	23.5	15.6	5.4	5.2	3.6	1.6
55.7	23.9	14.8	5.6	12.0	10.0	2.0
55.8	24.7	13.9	5.7	11.6	9.6	2.0
56.7	22.8	14.4	6.0	21.2	10.4	10.8
57.1	22.5	14.6	5.8	1.6	1.2	0.4
57.1	21.3	16.5	5.1	6.4	4.8	1.6
57.5	22.0	14.8	5.7	6.0	6.0	0
57.5	21.5	15.7	5.3	4.4	2.4	2.0

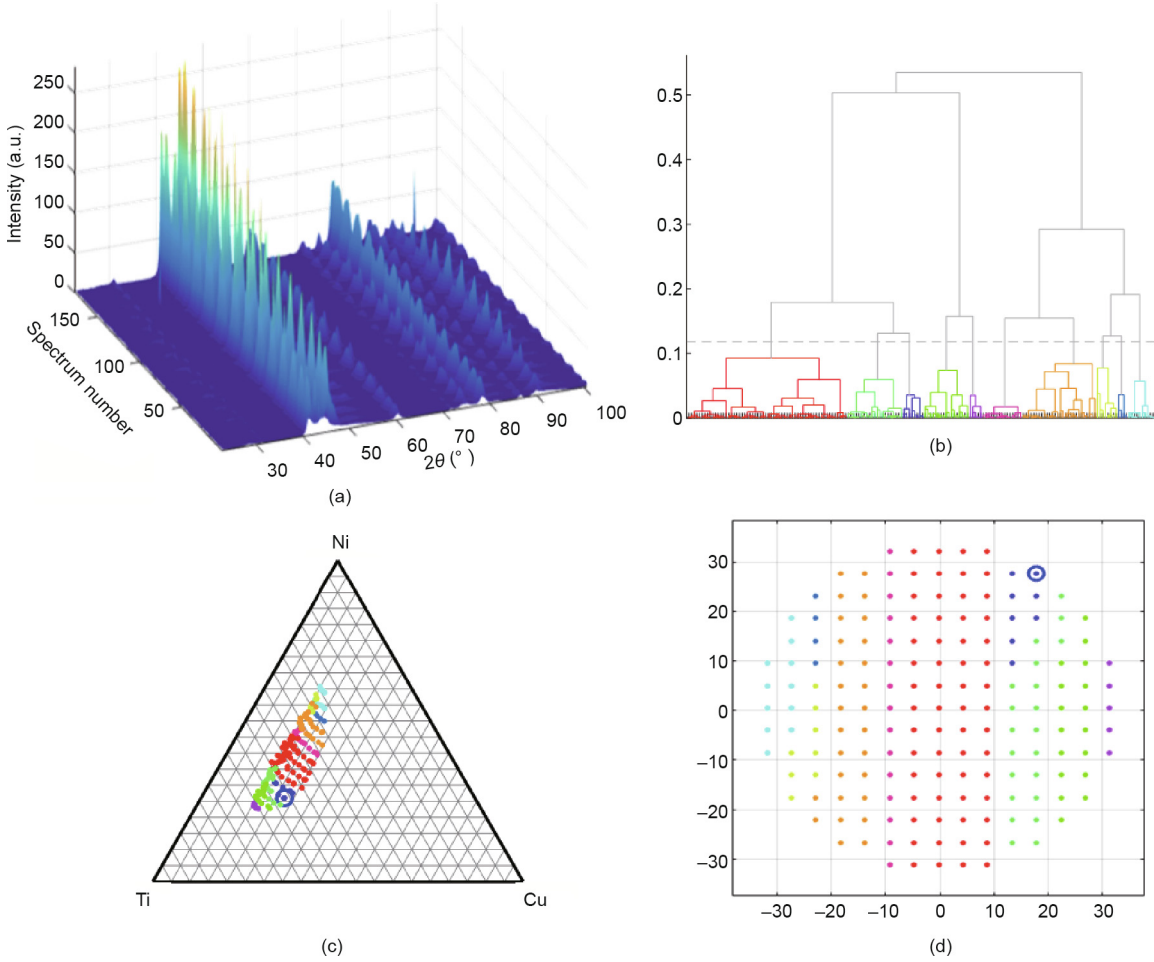

Fig. 4. Hierarchical cluster analysis of diffraction patterns for a quaternary thin-film library covering the range $[Ni_{36}–Ti_{52}–Cu_{12}]_{(100-x)}V_x$. The MATLAB-based data visualization platform CombiView allows linking of the sample position on the wafer with its composition and diffraction pattern, which is used to perform hierarchical cluster analysis to create a structural phase diagram. (a) 177 diffraction patterns with an *x*-axis of 2θ between 22° and 100°; (b) pearson correlation coefficient cluster analysis model showing grouping of XRD patterns based on similarities in peak positions; (c) composition space covered in this study as projected on a ternary plot of Cu–Ni–Ti with constant V identifying structural phase boundaries as delineated from hierarchical clustering shown in (b); (d) grouping by position on wafer (long flat edge at bottom).

Table 2
Overview of crystal structures identified in the Ni–Ti–Cu–V materials library.

Formula	Space group	Space group number	Prototype
NiTi	*Pm*-3*m*	221	$(Ti_{0.64}Zr_{0.36})$ Ni
$TiNi_{0.8}Cu_{0.2}$	$P2_1/m$	11	Monoclinic
CuNi i	*I*4/*mmm*	139	Tetragonal
$Ni_{0.25}Cu_{0.75}$	*Im*3*m*	229	
$Ti_2Co_{0.06}$	$P6_3/mmc$	194	Hexagonal
$(Cu_{0.03}Ni_{0.97})_3Ti$	$P6_3/mmc$	194	
$Ti(Ni_{2.79}Cu_{0.21})$	*R*-3*m*	166	Rhombo. H. axes
$TiNi_{0.8}Cu_{0.2}$	*Pmam*	51	Orthorhombic
$Ti(Cu_{0.053}Ni_{0.947})_3$	$P6_3/mmc$	194	
$(Ti_{0.67}V_{0.33})Ni_3$	$P6_3/mmc$	194	
Ti Ni_2 Cu	*Pmmn*	59	

$Ni_{0.25}$ $Cu_{0.75}$ and tetragonal CuNiTi phases were found in Ti-rich regions with the highest V content. The increased replacement of Ni by V was observed to stabilize the transformable cubic and tetragonal martensite variants (Fig. 5). A mix of cubic crystal structure having a prototype formula $(Ti_{0.64}Zr_{0.36})Ni$ and hexagonal $Ti(Cu_{0.053}Ni_{0.947})_3$ made up the majority of the composition space covered in this materials library having no transformation. For Ni-rich regions, orthorhombic phases of $TiNi_2Cu/TiNi_{0.8}Cu_{0.2}$ mixed with hexagonal $(Ti_{0.67}V_{0.33})Ni_3$ were identified as Ni content was reduced.

The addition of Cu to binary NiTi such that Cu replaces Ni has been shown to decrease the misfit between austenite and martensitic lattices. This translates to a slight decrease in M_s and reduced width of the thermal hysteresis, which, when combined, improves fatigue properties. The influence of the addition of V as a ternary element to NiTi was reported by Frenzel et al. [9], who demonstrated a reduction in M_s. In addition, the mechanical behavior was stabilized so that a small residual strain was maintained, compared with binary NiTi. Ni–Ti–Cu–V has been demonstrated for application as an elastocaloric material that is able to fulfill the potential of using $Ni_{45}Ti_{47.25}Cu_5V_{2.75}$ in ribbon form [26] and $Ni_{50}Ti_{45.3}V_{4.7}$ in a square prismatic form [27]. The identification of new compositions with reduced thermal hysteresis is a starting point for scale-up experiments to determine their long-term robustness through mechanical testing.

3.5. Effect of temperature cycling on film resistance

Thermal stability over many cycles is an important consideration in the optimization of heat transfer and the determination of functional fatigue, specifically, when using SMAs for elastocaloric cooling [28]. Film sheet resistance at room temperature (Fig. 6(a)) was measured prior to cycling the library between −40 and 120 °C for temperature-dependent resistance measurements. The

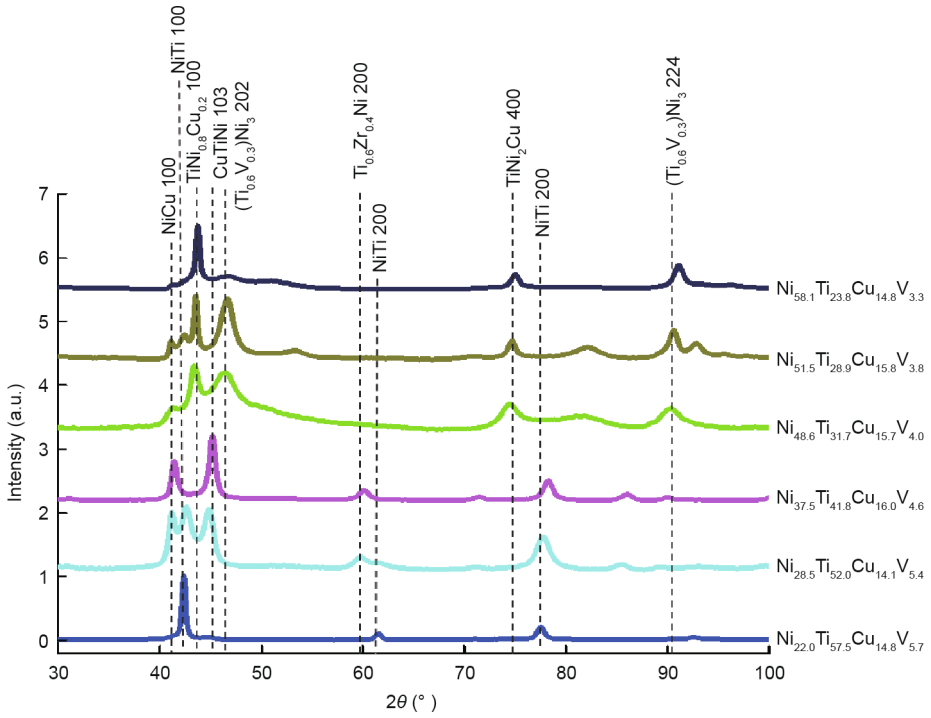

Fig. 5. Selected diffraction patterns representing the six clusters identified by the Pearson correlation coefficient clustering model. Substitution of Ni by V increases with distance from the abscissa, reflecting a shift in the non-transforming orthorhombic and hexagonal phase mixture to transformable cubic and tetragonal crystal structures. Patterns are offset for clarity.

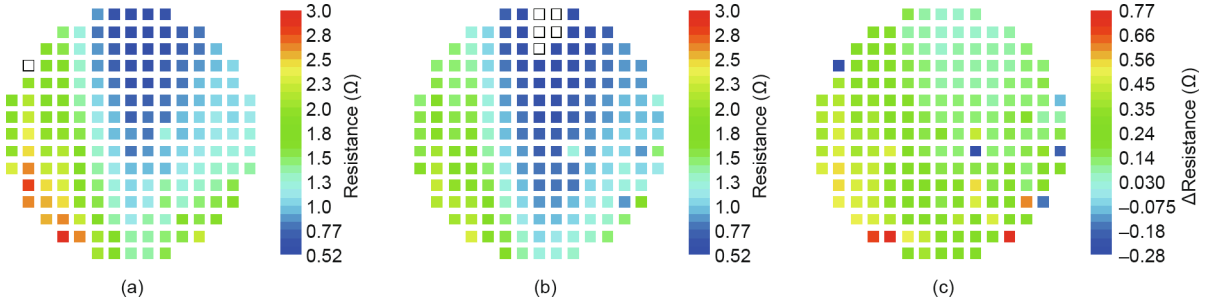

Fig. 6. Thin-film sheet resistance at room temperature (a) before and (b) after 84 temperature cycles between −40 and 120 °C. Post-cycling resistance was mapped using the same scale as pre-cycling; values outside of this range are indicated by colorless boxes. (c) Difference in resistance from (a) and (b). The color scale from red to blue indicates high to low values, respectively. The wafer was oriented with the long flat edge at the bottom.

effect of temperature cycling on film resistance was evaluated since the library was subjected to 84 temperature cycles, and is shown in Fig. 6(b) with the difference mapped in Fig. 6(c). While the SME was stable, as determined from the observation of transformation in Fig. 2, an overall reduction in sheet resistance was observed. XRD measurements collected post-thermal cycling show little to no change in diffraction patterns, thereby suggesting good structural stability (data not shown).

4. Conclusions

In this work, we report on the combinatorial thin-film synthesis and high-throughput characterization of a quaternary alloy. We provide an overview of the dependence of material properties on composition and structure through composition–structure–property maps. The Ni–Ti–Cu–V materials library we synthesized spans a composition region that has shape memory behavior. A strong correlation can be made between the microstructure and phase transformation property and, hence, composition. SMA effect is prominent in the Ti-rich region, with a significant number of compositions having near-zero thermal hysteresis. Increasing addition of V was observed to stabilize the mixture of cubic and tetragonal phases identified in compositions exhibiting SMA behavior. For non-transforming compositions, both linear and nonlinear $R(T)$ curves were observed, which were attributed to double-phase and low-symmetry crystal structures. SME and thermal hysteresis were stable over close to a hundred cycles. This work explored and validated the use of V as a fourth element in fine-tuning the operating temperature of a Ni–Ti–Cu ternary alloy in the ambient temperature regime for elastocaloric cooling applications. Work remains to be undertaken to understand the limits of V addition on the enhancement of efficiency and functional stability of the elastocaloric effect in NiTi alloys.

Acknowledgements

The author thanks Tieren Gao, Peer Decker, Alan Savan, and Manfred Wuttig for fruitful discussions. The authors gratefully

acknowledge funding support by the National Science Foundation Graduate Research Fellowship Program (DGE 1322106).

Compliance with ethics guidelines

Naila M. Al Hasan, Huilong Hou, Suchismita Sarkar, Sigurd Thienhaus, Apurva Mehta, Alfred Ludwig, and Ichiro Takeuchi declare that they have no conflict of interest or financial conflicts to disclose.

Appendix A. Supplementary data

Supplementary data to this article can be found online at https://doi.org/10.1016/j.eng.2020.05.003.

References

[1] Otsuka K, Wayman CM, editors. Shape memory materials. Cambridge: Cambridge University Press; 1998.
[2] Buehler WJ, Wang FE. A summary of recent research on the nitinol alloys and their potential application in ocean engineering. Ocean Eng 1968;1(1):105–20.
[3] Stöckel D. The shape memory effect: phenomenon, alloys, applications. In: Proceedings of the 1995 Shape Memory Alloys for Power Systems EPRI; 1995; Fremont, CA, USA; 1995. p. 1–13.
[4] Otsuka K, Ren X. Physical metallurgy of Ti–Ni-based shape memory alloys. Prog Mater Sci 2005;50(5):511–678.
[5] Lagoudas DC, editor. Shape memory alloys: modeling and engineering applications. Boston: Springer; 2008.
[6] Lobo PS, Almeida J, Guerreiro L. Shape memory alloys behaviour: a review. Procedia Eng 2015;114:776–83.
[7] Mohd Jani J, Leary M, Subic A, Gibson MA. A review of shape memory alloy research, applications and opportunities. Mater Des 2014;56:1078–113.
[8] Zarinejad M, Liu Y. Dependence of transformation temperatures of NiTi-based shape-memory alloys on the number and concentration of valence electrons. Adv Funct Mater 2008;18(18):2789–94.
[9] Frenzel J, Wieczorek A, Opahle I, Maaß B, Drautz R, Eggeler G. On the effect of alloy composition on martensite start temperatures and latent heats in Ni–Ti-based shape memory alloys. Acta Mater 2015;90:213–31.
[10] Otsuka K, Ren XB. Factors affecting the ms temperature and its control in shape-memory alloys. Mater Sci Forum 2002;394–395:177–84.
[11] Morgan N. Medical shape memory alloy applications—the market and its products. Mater Sci Eng A 2004;378(1–2):16–23.
[12] Petrini L, Migliavacca F. Biomedical applications of shape memory alloys. J Metall 2011;2011:1–15.
[13] Otsuka K, Kakeshita T. Science and technology of shape-memory alloys: new developments. MRS Bull 2002;27(2):91–100.
[14] Qian S. Development of thermoelastic cooling systems [dissertation]. Maryland: University of Maryland, College Park; 2015.
[15] Qian S, Geng Y, Wang Y, Pillsbury TE, Hada Y, Yamaguchi Y, et al. Elastocaloric effect in CuAlZn and CuAlMn shape memory alloys under compression. Philos Trans R Soc A Math Phys Eng Sci 2016;374(2074):20150309.
[16] Chluba C, Ge W, Lima de Miranda R, Strobel J, Kienle L, Quandt E, et al. Ultralow-fatigue shape memory alloy films. Science 2015;348(6238):1004–7.
[17] Vasile SI, Grabowska KE, Ciesielska-Wrobel I, Ghitaiga J. Analysis of hybrid woven fabrics with shape memory alloys wires embedded. Fibres Text East Eur 2010;18(1):64–9.
[18] Xue D, Xue D, Yuan R, Zhou Y, Balachandran PV, Ding X, et al. An informatics approach to transformation temperatures of NiTi-based shape memory alloys. Acta Mater 2017;125:532–41.
[19] Xue D, Balachandran PV, Hogden J, Theiler J, Xue D, Lookman T. Accelerated search for materials with targeted properties by adaptive design. Nat Commun 2016;7(1):1–9.
[20] Cui J, Chu YS, Famodu OO, Furuya Y, Hattrick-Simpers J, James RD, et al. Combinatorial search of thermoelastic shape-memory alloys with extremely small hysteresis width. Nat Mater 2006;5(4):286–90.
[21] Zarnetta R, Takahashi R, Young ML, Savan A, Furuya Y, Thienhaus S, et al. Identification of quaternary shape memory alloys with near-zero thermal hysteresis and unprecedented functional stability. Adv Funct Mater 2010;20(12):1917–23.
[22] Van der Pauw LJ. A method of measuring specific resistivity and Hall effect of discs of arbitrary shape. Philips Res Rep 1958;13(1):1–9.
[23] Thienhaus S, Zamponi C, Rumpf H, Hattrick-Simpers J, Takeuchi I, Ludwig A. High-throughput characterization of shape memory thin films using automated temperature-dependent resistance measurements. MRS Proc 2006;894:197.
[24] Mueller T, Kusne A, Ramprasad R. Machine learning in materials science: recent progress and emerging applications. Rev Comput Chem 2016;29:186–273.
[25] Long CJ, Hattrick-Simpers J, Murakami M, Srivastava RC, Takeuchi I, Karen VL, et al. Rapid structural mapping of ternary metallic alloy systems using the combinatorial approach and cluster analysis. Rev Sci Instrum 2007;78(7):072217.
[26] Schmidt M, Ullrich J, Wieczorek A, Frenzel J, Schütze A, Eggeler G, et al. Thermal stabilization of NiTiCuV shape memory alloys: observations during elastocaloric training. Shape Mem Superelasticity 2015;1(2):132–41.
[27] Kim Y, Jo MG, Park JW, Park HK, Han HN. Elastocaloric effect in polycrystalline $Ni_{50}Ti_{45.3}V_{4.7}$ shape memory alloy. Scr Mater 2018;144:48–51.
[28] Bechtold C, Chluba C, Lima de Miranda R, Quandt E. High cyclic stability of the elastocaloric effect in sputtered TiNiCu shape memory films. Appl Phys Lett 2012;101(9):091903.